ELECTRON CLOUD BUILD-UP SIMULATIONS USING ECLOUD

D. Schulte* and F. Zimmermann
CERN, AB Department, Geneva, Switzerland

Abstract

The paper gives an overview of the status of electron cloud build-up simulations at CERN, using the ECLOUD code. The recent code modifications will be mentioned and comparisons of simulation results with measurements in the SPS will be discussed. Finally some prediction of the electron cloud for the LHC will be given.

INTRODUCTION

Understanding of the electron cloud effect requires tools capable of simulating the build-up of the cloud. One such tool is ECLOUD, which was developed by various authors [1] over a number of years [2, 3, 4, 5, 6]. This fortran code can only run on a single CPU and does not use most of the modern algorithms. However, it uses little resources; an SPS train of 72 bunches can be simulated in about half an hour on an old desktop PC (1-GHz pentium-III) and requires only 15 MB of memory.

In the past year a number of corrections and improvements of the code have been performed and we will give a short overview over these developements. In addition a number of experiments in the SPS have been performed to help benchmark the predictions of the simulations, which we will also present.

If not otherwise stated all the simulations have been performed for an LHC type beam in the SPS, with an intensity of 11×10^{10} protons per bunch and 72 bunches per train. The other beam parameters have been determined by G. Arduini on the basis of the logged data [7].

A simulation of the build-up of the electron cloud consists of four main areas.

- The simulation of the interaction of the electrons with the surface and the secondary particle production.
- The calculation of the fields in the beam pipe including those produced by space charge.
- The tracking of the particles through these fields.
- The simulation of additional effects, namely of the detectors used in the experiment.

In the following, the improvements in these areas are detailed.

* Daniel.Schulte@cern.ch

SECONDARY EMISSION

The results of electron cloud simulations depend strongly on the assumed model for the secondary emission. We present the model used and describe a potential experiment which may help to constrain the model for the reflection of low energy electrons in the SPS.

Modelling

In ECLOUD two different contributions to secondary emission exist, true secondaries and reflected electrons. So-called re-diffused electrons, whose spectrum would cover an intermediate energy range, are not separately considered in the ECLOUD code.

Thus, the total secondary emission yield is expressed as the sum of two components:

$$\delta_{\rm tot}(E_p,\theta) = \delta_{\rm true}(E_p,\theta) + \delta_{\rm el}(E_p)\ . \qquad (1)$$

It is a function of the energy of the primary electrons, E_p and of the impact angle with respect to the surface normal, θ. In the present version of the code, the elastic component is assumed not to depend on the angle, since no data are available for incidence directions other than perpendicular and since both local surface roughness as well as isotropic crystal orientations are expected to wash out any dependence expected for monocrystals. We first discuss the true secondaries, then the elastically reflected component.

The true secondary yield as a function of the primary impact energy E_p is expressed by the Furman formula [8]

$$\delta_{\rm true}(E_p) = \delta_{\rm max}(\theta)\frac{s\frac{E_p}{E_{\rm max}}}{s-1+(\frac{E_p}{E_{\rm max}})^s}\ , \qquad (2)$$

where $s \approx 1.35$ and the two adjustable parameters $\delta_{\rm max}$ and $E_{\rm max}$ describe the maximum yield and the energy at which it is attained. The dependence on the angle θ is inferred from laboratory measurements as [8]

$$E_{\rm max}(\theta) \approx E^0_{\rm max}(1+0.7\,(1-\cos\theta)) \qquad (3)$$

and [9]

$$\delta_{\rm max}(\theta) \approx \delta^0_{\rm max}\exp(0.5\,(1-\cos\theta))\ , \qquad (4)$$

where quantities with superscript 0 refer to perpendicular incidence.

The values of $\delta^0_{\rm max}$ and $E^0_{\rm max}$ characterize the degree of conditioning. In-situ measurements at the SPS in 2002 and 2003 indicated $\delta^0_{\rm max} \approx 2.35$ and $E^0_{\rm max} \approx 260$ eV for the

initial state, and $\delta^0_{\rm max} \approx 1.5$ and $E^0_{\rm max} \approx 240\,$eV after a 10-day 'scrubbing' run [10]. In laboratory measurements samples are fully conditioned after depositing an electron dose of $10\,$mC/mm^2. The final conditioning effect may depend not only on the total dose, but also on the electron flux during the processing [11]. Conditioned laboratory samples typically exhibit final maximum emission yields as low as $\delta^0_{\rm max} \approx 1.1$. For simulation purposes, the value of $E^0_{\rm max}$ corresponding to other values $\delta^0_{\rm max}$ is estimated by linear interpolation from the above numbers obtained in the SPS (see Table 1).

The energy distribution of the true secondaries is concentrated at low energies, and can be parametrized as in Ref. [12], namely

$$D(E_s) \propto \exp\left(-\frac{(\ln\frac{E_s}{E_0})^2}{2\tau^2}\right) , \qquad (5)$$

where $E_0 \approx 1.8\,$eV and $\tau \approx 1$ are two fitting parameters. For this distribution, the average emission energy of the true secondaries is $\bar{E}_s \approx 8.1\,$eV.

The initial angular distribution of the secondaries in spherical coordinates, $dN/d\Omega$, is taken to be of the form $\cos\theta$, where θ denotes the emission angle of the secondary electron with respect to the surface normal [13].

The elastically reflected component of the secondary electrons is significant at low impact energy. Based on the experimental data in [14], the electron elastic reflectivity is assumed to be unaffected by the conditioning process, and to always approach the value of 1 in the limit of zero primary energy. The measurements of elastic reflection in [14] are very well parametrized by

$$\delta_{\rm el}(E_p) = \frac{(\sqrt{E_p+E_0}-\sqrt{E_p})^2}{(\sqrt{E_p+E_0}+\sqrt{E_p})^2} . \qquad (6)$$

This formula for $\delta_{\rm el}$ can be obtained from a simple quantum-mechanical model [15], considering a plane-wave electron wave function incident on a negative potential step of depth E_0. The value for the single adjustable parameter, $E_0 \approx 150\,$eV, was derived by a fit to the measurements [14]. The expression for $\delta_{\rm el}$, (6), gives rise to a minimum in the total secondary yield, at around $10\,$eV, consistent with many of the experimental data, *e.g.*, those published in Refs. [14] and [12].

Figure 1 displays curves of the total secondary emission yield at perpendicular and shallow impact, as well as of its two components, as a function of the primary electron energy, corresponding to the parameter values $\delta^0_{\rm max} = 1.5$ and $E^0_{\rm max} = 235.5\,$eV. The reflection probability equals one for incident energies approaching zero, so that the total yield exhibits a minimum near $10\,$eV. Table 1 lists typical secondary-emission parameters used for simulating electron-cloud build up in the LHC before and after scrubbing.

Table 1: Typical simulation parameters related to secondary emission.

parameter	initial	final
max. sec. emission yield $\delta^0_{\rm max}$	1.9	1.1
energy of maximum yield, $\epsilon^0_{\rm max}$	249 eV	230 eV
parameter for elast. el. reflection E_0	150 eV	150 eV

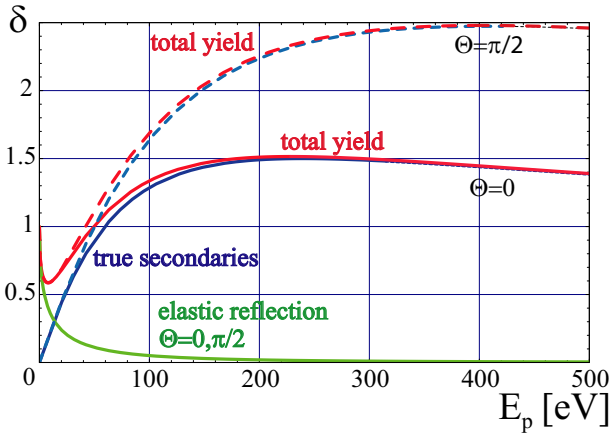

Figure 1: Model of the total and secondary emission yield $\delta_{\rm tot} = \delta_{\rm true} + \delta_{\rm el}$ (red) and the true secondary yield $\delta_{\rm true}$ (blue), at perpendicular ($\theta = 0$, solid lines) and shallow incidence ($\theta = \pi/2$, dashed lines), as a function of the primary electron energy for $\delta^0_{\rm max} = 1.5$, $E_{\rm max} = 239.5\,$eV); the partial yield from elastic reflection $\delta_{\rm el}$ is also displayed (green); the elastic reflection is assumed to be independent of the angle of incidence.

A Potential Experiment

A possibility to gain experimental data on the low energy reflection could be the measurement of survival time of "seed electrons" as explained below. For high enough beam intensity, the electron cloud builds up during the passage of the bunch train until it reaches saturation level after a given number of bunches, see Fig. 2. If a second train follows the first with some distance, saturation will be reached within a smaller number of passing bunches of this train. This results from the fact that low energy electrons survived the gap between the trains and serve as seeds for the cloud build-up in the next train. The number of bunches passing before saturation in the second train depends on the train distance as well as on the reflectivity; for smaller reflectivity the electrons will be lost more quickly.

Figure 3 illustrates the effect. It can be seen that the difference between 100% and 50% reflectivity is quite large while the latter is not too different from no reflectivity at all. Performing such an experiment in the SPS should be relatively straightforward and can be very useful in constraining the model.

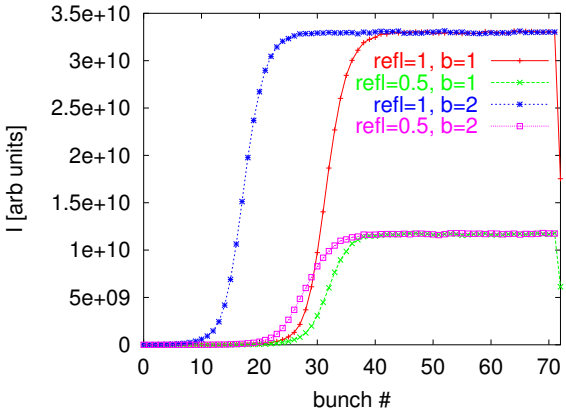

Figure 2: The build-up of the electron cloud along the first (b=1) and second (b=2) bunch train. The distance between trains is 3μs; 100% and 50% reflectivity for low energ electrons was assumed, respectively.

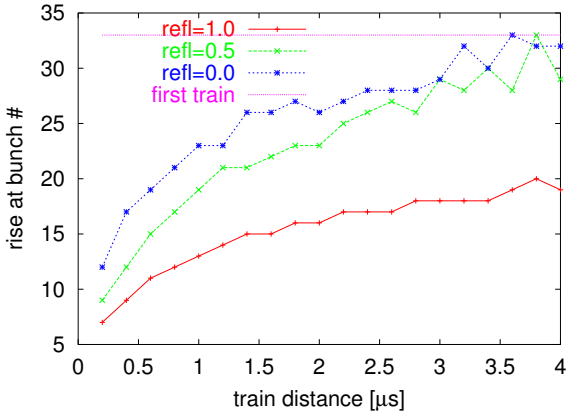

Figure 3: The number of bunches passing before the electron cloud density reaches 50% of the saturation level. An SPS beam with nominal LHC bunch charges is used.

BOUNDARY CONDITIONS

The fields produced by the beam and the electron depend cloud on the shape of the beam pipe and the image currents and charges on it's inner surface. Different shapes can be simulated in ECLOUD:

- a round beam pipe
- an elliptical beam pipe
- an elliptical beam pipe with a flat upper and lower part, corresponding to the LHC beam pipe, see below
- a rectangular beam pipe.

A number of improvements of the field calculations have been performed and a number of errors have been detected and removed. The speed of calculations with elliptical boundaries has been improved by an order of magnitude due to different code changes. The effect of rectangular

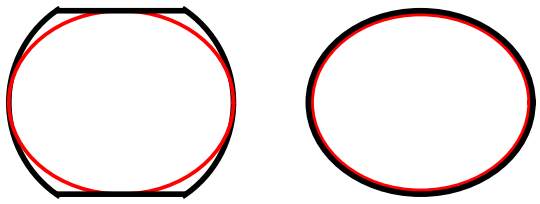

Figure 4: The two old models used for the simulation of the LHC beam pipe. The black boundary corresponds to the one used to simulate the secondary emission. The red boundary is used for the calculation of the space charge fields.

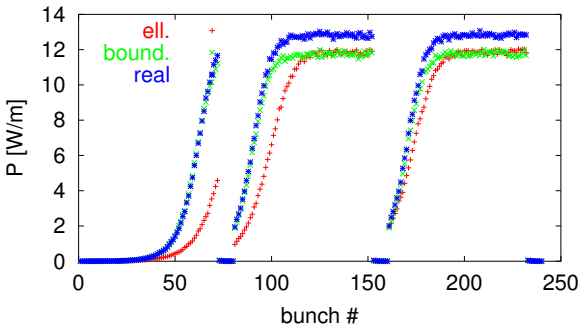

Figure 5: The build-up of the electron cloud along the bunch train for $N = 12 \times 10^{10}$. The time to reach full saturation is model-dependent, the final level of the electron cloud is much less dependent.

boundaries has been fully implemented. Finally, a new interface for space charge has been integrated which allows to more realistically model the LHC beam pipe.

The LHC Beam Pipe Models

The LHC has a round beam pipe that has a flat upper and lower part, see Fig. 4.

In the previous version of the code the LHC boundaries could only be simulated by using the real beam pipe for the secondary emission and an inscribed ellipse as the electrical boundary. Figure 4 illustrates this. On the left side the black curve shows the boundary used for the secondary emission, while the red line shows the boundary used for the field calculation. In order to use a more coherent description, ellipses have been used for the beampipe as well as the electrical boundaries, see the right part of Fig. 4. In many cases the results are very similar. Differences however can exist; in particular for the rise time of the cloud, see Figs. 5 and 6. To cross check these simulations ECLOUD was extended to be able to read the coefficients for the space charge calculations from a file. This file can be prepared using a new code.

This code solves the potential produced by the charges

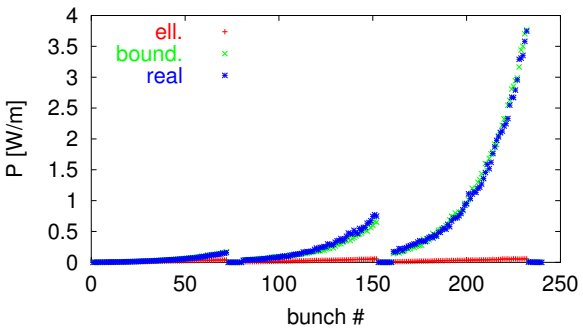

Figure 6: The build-up of the electron cloud along the bunch train for $N = 16 \times 10^{10}$, illustrating that in particular cases the electron cloud strongly depends on the beam pipe model.

in free space by applying the convolution theorem and fast Fourier transformation. It then determines the charges necessary on the boundary in order to achieve zero potential at the boundary. Finally it calculates the potential created by these charges in all the other cells, using again the convolution theorem.

TRACKING

Different routines are used to track the electrons of the cloud depending on the type of magnetic field in the beam pipe. In the case without magnetic field the tracking is straightforward, while it can be quite time consuming in the cases with a magnetic field, since the low energy electrons are strongly affected. In order to speed up the program the tracking was modified for two different magnetic fields.

Tracking in Dipole Fields

The tracking in a dipole field had been performed using a partial differential equation integrator. However, the trajectory can be determined analytically. The program has been changed accordingly improving the speed by about an order of magnitude.

Tracking in Quadrupole Fields

Simulation of a quadrupolar field is by far the most time consuming of the cases relevant for the LHC. A first step was to exchange the partial differential equation solver by a faster algorithm based on Bulirsch-Stoer, gaining a factor of two in overall program speed. A dedicated tracking routine however proved to yield even better performance (about 8.5 times faster than the initial code). The routine uses adaptive step sizes. Each time intervall is passed several times, with an increased number of steps. For each step the fields are assumed to be locally homogeneous, so that the particle moves on a helix. The results of the different passages of the same time intervall are then extrapolated to an infinite number of steps: the final result. The procedure is similar to the Bulirsch-Stoer integration, but takes advantage of the analytic solution for a homogeneous field.

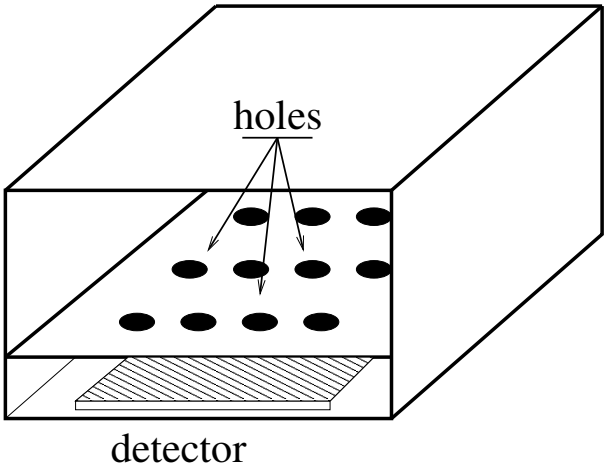

Figure 7: A sketch of the beam pipe with the detector.

DETECTOR MODELLING

To ensure correct comparison of experimental data and the code it is necessary to model the detectors in some detail. In case of the strip detector [16], effects can be expected from the bias voltage and the fact that particles that are detected are removed from the cloud. This is in particular the case for high magnetic dipole fields where particles tend to spiral around the field lines.

Model of the Detector

A simplified sketch of the detector is shown in Fig. 7. The actual detector is at the bottom separated from the beam by a metal sheet with holes. Only electrons which pass through these holes can be detected. In the simulation, the distance between the holes and the detector is neglected, a particle which hits a hole will be registered. The bias voltage is taken into account by comparing the vertical kinetic energy of the electrons that hits a sensitive spot with the potential difference given by the bias voltage. If it is larger the particle can be detected and removed from the cloud, otherwise it will be reflected.

To illustrate the effect of the detector four simulations have been performed. For a case with no bias voltage the detected current has been calculated assuming that the electrons which hit the sensitive spots produce secondaries as at any other position. The same simulation has been repeated with the realistic assumption that detected particles are removed from the cloud. As can bee seen in Fig. 8 the registered flux is quite different from the one measured before. Obviously the detector changes the flux in the sensistive areas as compared to the uninstrumented case.

A similar simulation has been performed for the case where a bias voltage is applied. It shows a significantly smaller dependence of the measured flux on the detector

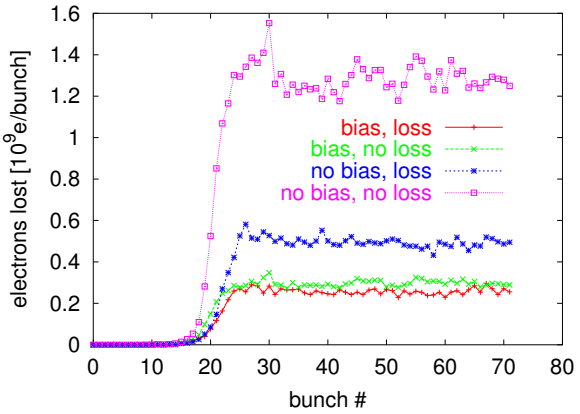

Figure 8: The number of electrons lost per passing bunch for nominal beam in a 0.01 T dipole field. In one case a 20 V bias voltage was applied in the other not.

effect, see Fig. 8.

Dependence of the Flux on a Magnetic Field

The modelling of the detector can improve the agreement between simulation and experiment as shown below.

In the SPS some measurements have been performed to determine the electron flux on the beam pipe wall for different magnetic fields and beam intensities. The detector had no bias voltage and consequently a significant dependence on of the measurement on the field is to be expected. Figure 9 shows the comparison of the measured data and the simulations. Since no calibration of the measurement exists only the relative signals can be compared. In the case of the simulation without detector effects, the agreement is very good for small fields. The measurement however shows a much faster suppression of this flux at higher fields than the simulation. If one takes into account the detector effects, better agreement is found for high fields. However the agreement is still not perfect.

SIMULATION OF THE SCRUBBING

The beam pipe surface of a machine experiencing electron cloud will be scrubbed by the electron cloud. This leads to a reduction of the secondary emission yield and consequently will reduce the electron cloud effects. The scrubbing is a local effect and depends on the electron dose collected at a surface. The full simulation of this process can be important. First, the fact that the secondary emission yield is not constant on the whole surface can affect measurements, e.g., those comparing the electron flux with and without magnetic field, since the relevant areas of the surface are different for the two cases. Second, understanding the local secondary emission yield may help to improve the scrubbing procedure for the LHC, where one wants to scrub the relevant surface areas as quickly as possible. In the following, a first simulation of the scrubbing procedure is presented.

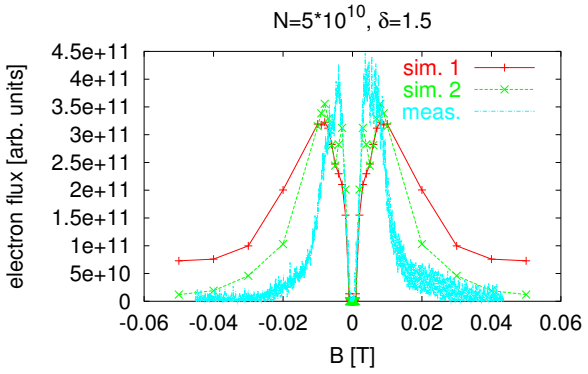

Figure 9: The electron flux as a function of the magnetic field in a detector with no bias voltage. No absolute calibration of the measurment exists, so only the functional dependence can be compared. The simulation (with $\delta_{max} = 1.5$) of the flux which does not take the detector effect into account (labeled sim. 1) shows good agreement for small fields but not for large fields. Taking into account the detector effects (labeled sim. 2), significantly improves the agreement between measurement and simulation yet the agreement is not perfect.

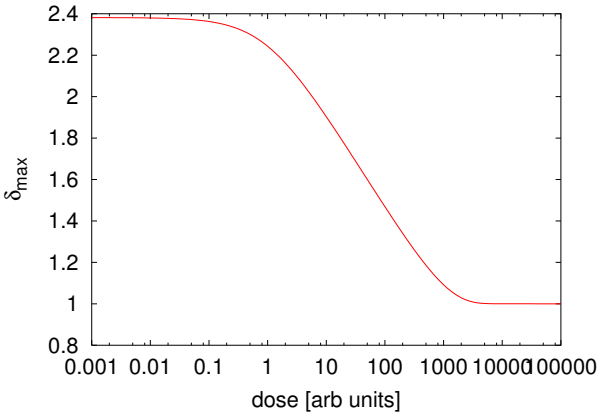

Figure 10: The model of the dependence of secondary emission yield on the accumulated electron dose.

Simulation Procedure

For the simulations `ECLOUD` has been modified. The beam pipe surface is transversely cut into 200 areas, each of which can have a different secondary emission yields. These yields can be read from a file. The accumulated electron dose in the different areas is written to a file and be used to determine the change in the local secondary emission yield. Here, a simple model for the dependence of the secondary emission yield on the accumulated dose is used; it is illustrated in Fig. 10. Initially the whole surface is assumed to have collected no dose. The simulation is performed as follows: First `ECLOUD` is executed to calculate the flux at the surface. Then the change of secondary emission yield is calculated based on the flux. (The dose

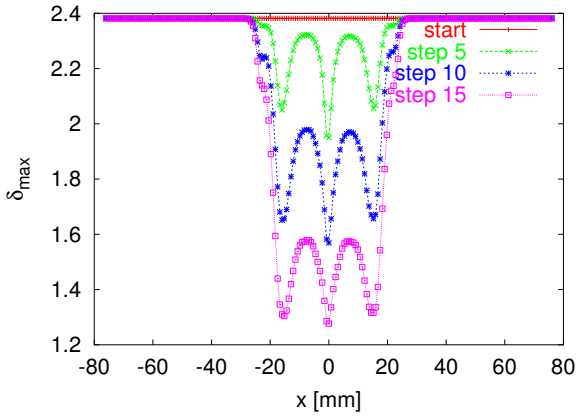

Figure 11: The model of the dependence of secondary emission yield on the accumulated electron dose.

accumulated locally per simulation step is scaled so as to avoid changes of the seconday emission yield of more than 0.1). This procedure is iterated a number of times. The evolution of the secondary emission yield is shown in Fig. 11 for a beam pipe in a dipole field of $B_y = 0.01$ T.

Sample Result

The effect of the scrubbing on the flux measurement is illustrated in Fig. 12. The simulation of the scrubbing has been performed as described above. The build-up of the actually resulting secondary emission yield distribution along the train has then been compared to the build-up assuming a constant yield at the whole surface. A value of $\delta_{\max} \approx 1.4$ reproduces the real distribution quite well. Assuming the same scrubbed machine but that the measurement is performed with no field, one can also get good agreement between a constant yield and the real distribution, this time at a value of $\delta_{\max} \approx 1.9$.

It is clear that the history of the scrubbing procedure has a very important impact on the measurment results and that comparisons of the flux with and without field can be quite complicated.

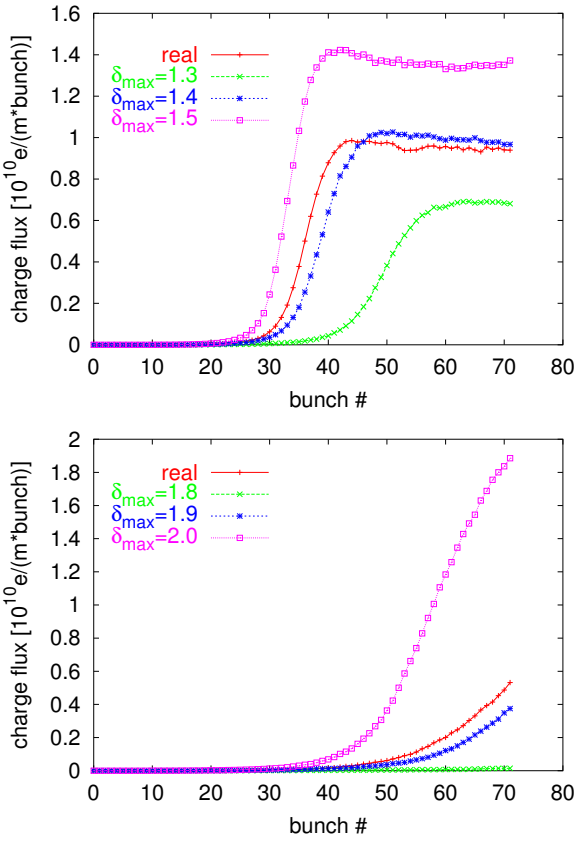

Figure 12: Comparison of the electron cloud build-up along a bunch train for a machine where the surface has a constant secondary emission yield and one where the yield depends on the scrubbing due to the previous electron flux. The scrubbing was performed in a dipole field of $B_y = 0.01$ T. Top: Build-up in case no field is applied during measurement. Bottom: Build-up in case of a dipole field $B_y = 0.01$ T during measurement. The equivalent constant secondary yields are very different for the two cases.

FURTHER BENCHMARKING AT THE SPS

An entire suite of detectors in the SPS [16, 17] allows for a number of independent benchmarks between simulations and measurements. In addition to the absolute flux of electrons at the wall with and without dipole field, and to the effect of a magnetic field on the spatial extent of the cloud, which were discussed above, it is also possible to compare the energy spectra of electrons hitting the wall, the heat load deposited, and the dependence of the spatial structure of the electron cloud on the bunch intensity.

Figure 13 compares the measured energy distribution at a 'strip detector' with simulated spectra for two different values of $\delta_{\max}$ and two different rms bunch length. Again the detector bias voltage of 30 eV was taken into account in the simulation. Though the agreement is not yet perfect, it appears that for an rms bunch length of 0.225 m and $\delta_{\max} = 2.0$ both the maximum energy in the spectrum, near 700 eV, and the position and height of the maximum at 200 eV are well reproduced. A more detailed simulation of the detector may resolve the remaining differences.

In a dipole field of the SPS, the multipacting occurs in the form of one, two, or three vertical stripes, depending on the bunch intensity. The position of the stripes reflects regions with maximum electron amplification, which arise due to the combined effect of the electric beam field, its image field, the magnetic field, and the chamber geometry. Figure 14 illustrates the simulated horizontal distance of one of the two stripes from the central position of the beam for the SPS strip detector. Two sets of measured data taken in 2001 and 2002 are superimposed. These had been compared successfully before, using an older version of the code. The new comparison confirms the good agreement,

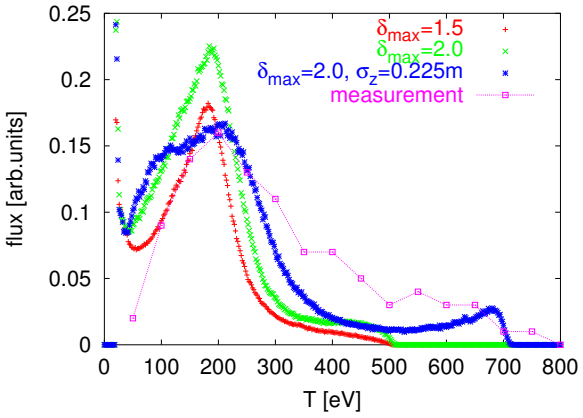

Figure 13: Measured and simulated energy spectra for the strip detector; the three simulation curves refer to different values of $\delta_{\max}$ and the rms bunch length; measurement data are a courtesy of M. Jiménez.

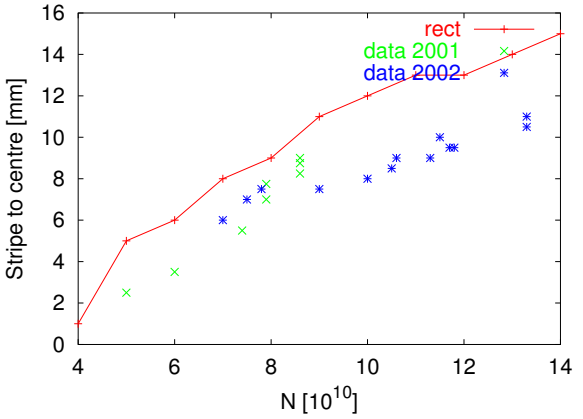

Figure 14: Measured and simulated horizontal distance of the vertical electron stripes (representing regions with high multipacting) from the center of the strip detector; are a courtesy of M. Jiménez.

though significant changes to the code were performed in the meantime.

Several calorimeters are installed in the SPS [18] whose purpose is to detect the heat load deposited by electrons impinging on the chamber wall, a critical effect for the LHC. WAMPAC1 is a warm copper calorimeter with a large round chamber (70 mm radius) [18]. WAMPAC3, a similar calorimeter, has about two times smaller transverse size (33.5 mm radius).

Figure 15 shows the simulated heat load as a function of the secondary emission yield for a bunch spacing of 25 ns and a bunch intensity of 1.15×10^{11} protons, assuming the estimated vacuum pressure of 100 nTorr. The measured value, also indicated, is consistent with $\delta_{\max} \approx 1.5$, the value also expected from a direct in-situ measurement of the secondary emission yield [16] at a different location in the SPS. For a larger bunch spacing of 75 ns, a detectable heat load was neither predicted by the simulations for 3

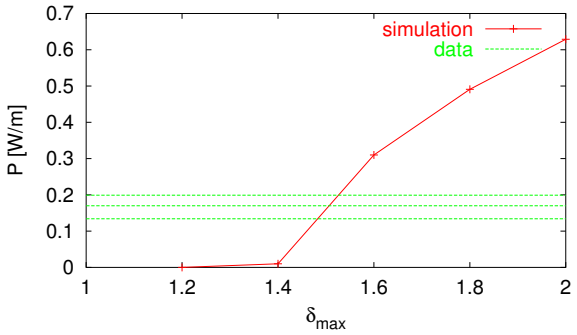

Figure 15: Simulated heat load in WAMPAC1 with 2 batches and 25-ns spacing as a function of $\delta_{\max}$ together with the heat load measured in 2002; experimental data courtesy of V. Baglin and B. Jenninger.

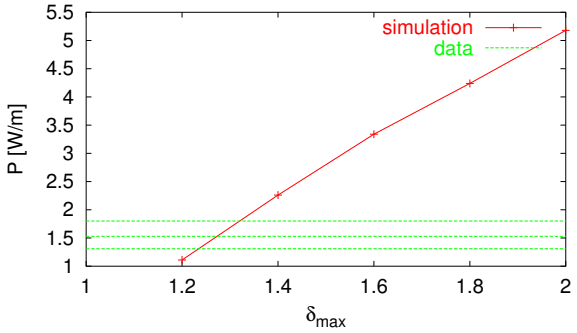

Figure 16: Simulated heat load in WAMPAC3 with 4 batches and 25-ns spacing as a function of $\delta_{\max}$ together with the heat load measured in 2003; experimental data courtesy of V. Baglin and B. Jenninger.

batches and $\delta_{\max} < 1.75$, nor measured in the experiment (resolution limit 20 mW/m).

Similar simulations were performed for WAMPAC3 with 4 batches, 25-ns spacing and about 50 nTorr pressure. Good agreement is obtained with measurements in 2003, if $\delta_{\max} \approx 1.3$, as is illustrated in Fig. 16. For WAMPAC3, a problem is however encountered in the case of 75 ns spacing and 3 batches. Figure 17 shows that the simulation predicts much less heat load than has been measured. Consistency could be achieved only for an unreasonably high value of $\delta_{\max} > 2.3$, which on the other hand would be in an eclatant contradiction to the 25-ns result. An additional heat source, not yet identified, might be one possible explanation.

PREDICTIONS FOR THE LHC

A primary concern for the LHC is the additional heat load deposited by the electron cloud on the beam screen (a Cu-coated stainless steel shield inserted into the arc vacuum chamber, which absorbs the photons from synchrotron radiation). Only a limited cooling capacity is available for the additional heat load due to the electron cloud. If it is

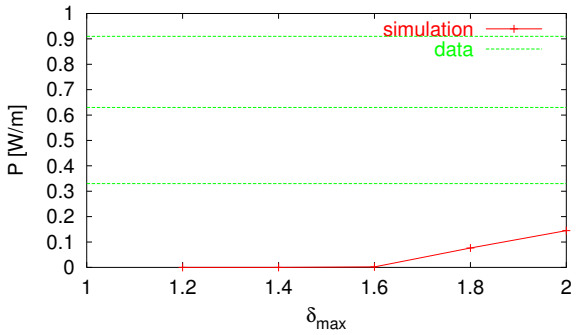

Figure 17: Simulated heat load in WAMPAC3 with 3 batches and 75-ns spacing as a function of $\delta_{\max}$ together with the heat load measured in 2003; experimental data courtesy of V. Baglin and B. Jenninger.

surpassed, a quench of the superconducting magnets would result.

Figures 18 and 19 show the heat load per unit length simulated for an LHC arc cell at injection energy and in collision, respectively. Each heat-load value was computed as a weighted average of three independent simulations for dipoles, field-free regions, and quadrupoles, according to the fraction of the cell length covered by each type of field (for sextupoles we assumed the same heat load as for quadrupoles). The various curves refer to different values of the maximum secondary emission yield, ranging from 1.1 to 1.7, and to different numbers of successive bunch trains.

In Figs. 18 and 19 an estimate of the cooling capacity available for the electron cloud is also indicated. It decreases towards higher intensity, since the cooling required for synchrotron radiation, image currents, and gas scattering increases. The latter process is here assumed to be dominant.

The LHC beam consists of batches of 72 bunches with 25-ns bunch spacing, which are separated by gaps of 225 ns. At injection energy, the multipacting process is launched by residual-gas ionization, and the electron build up saturates only at the end of the first or during the second batch. As a result, the simulated heat load depends on the number of batches. At top energy, photoelectrons are abundant and the electron density saturates already after a few bunches of the 1st batch, so that in this case the heat load is rather insensitive to the number of batches. Figure 18 suggests a resonance with enhanced heat load for bunch populations around 6×10^{10} protons, visible for the lower values of secondary emission yield. This picture also shows that with a maximum secondary emission yield of 1.3 it is possible to reach or exceed the nominal bunch intensity of 1.15×10^{11} at injection. On the other hand, a maximum emission yield below 1.1 is needed at top energy (Fig. 19).

Prior to achieving the low values of the secondary emission yield required for nominal performance by surface scrubbing, the LHC could be operated with a reduced

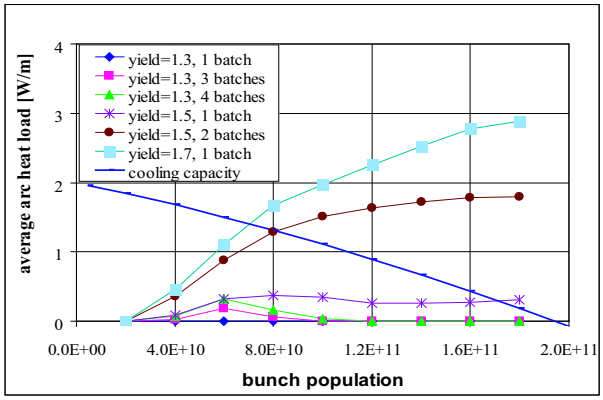

Figure 18: Simulated average arc heat load as a function of the bunch population for a bunch spacing of 25 ns at injection (450 GeV), considering various values of $\delta_{\max}$ and computing the heat load over several numbers of consecutive 72-bunch trains.

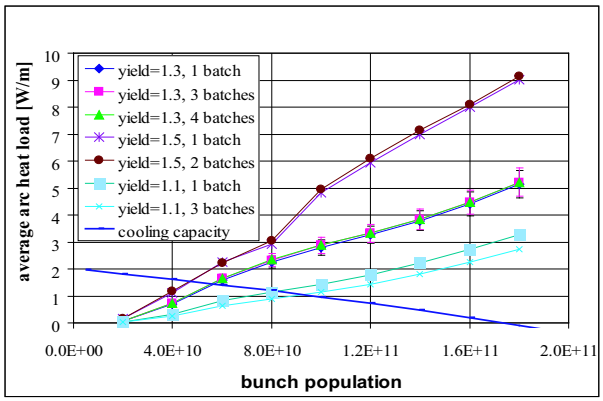

Figure 19: Simulated average arc heat load as a function of the bunch population for a bunch spacing of 25 ns at top energy (7 TeV), considering various values of $\delta_{\max}$ and computing the heat load over several numbers of consecutive 72-bunch trains.

charge per bunch (equal or below 5×1010 protons) or with an increased spacing between bunches. Simulated heat loads for 25 and 75-ns bunch spacing as a function of $\delta_{\max}$ are compared in Figs. 20 and 21. at injection and top energy, respectively. Here, a single batch and the nominal bunch population of 1.15×10^{11} were cnsidered. With 75-ns spacing, any realistic value of $\delta_{\max}$ can be accommodated, up to $\delta_{\max} = 2.0$ or beyond.

BUNCH-TO-BUNCH WAKE FIELD

As a by-product of the electron-cloud build up simulations, the transverse bunch-to-bunch wake field can also be obtained by the ECLOUD code. To this end, one bunch of the train is displaced transversely and the resulting force on the next bunch is computed, as it was done already by Ohmi [19].

The ECLOUD wake calculation for the SPS is rather noisy,

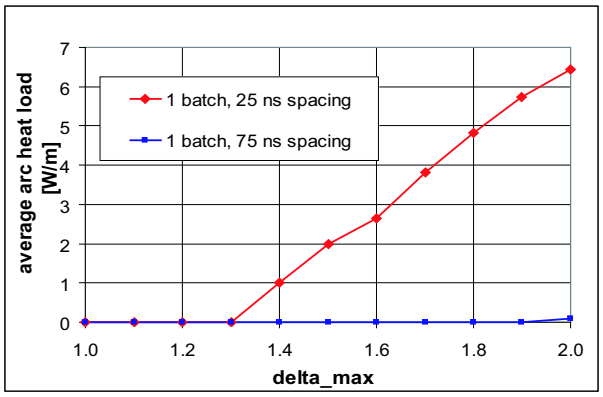

Figure 20: Simulated average arc heat load as a function of the maximum secondary emission yield for bunch spacings of 25 ns and 75 ns at injection (450 GeV), assuming the nominal bunch population of 1.15×10^{11}.

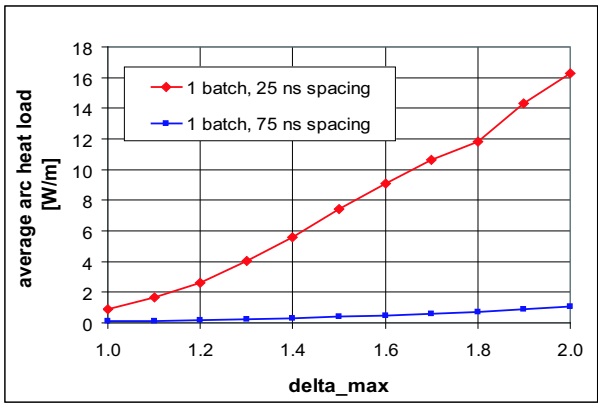

Figure 21: Simulated average arc heat load as a function of the maximum secondary emission yield for bunch spacings of 25 ns and 75 ns at top energy (7 TeV), assuming the nominal bunch population of 1.15×10^{11}.

and reliable numbers require the averaging over many simulation runs. Figures 22 and 23 present example results, which illustrate that the force experienced by the following bunch increases linearly with the displacement of the driving bunch, and that, hence, a constant wake field can be uniquely determined, as for a conventional impedance. Figure 23 is a magnified view of Fig. 22, which reveals a change of sign in the wake during the passage of the test bunch. We speculate that such type of coupled-bunch wake could easily drive coupled-bunch head-tail instabilities.

CONCLUSION

A number of corrections to the ECLOUD code have been implemented. The program speed has been improved by about an order of magnitude and the modelling of the beam pipe geometry and detector effects has advanced. A number of comparisons between experiment and simulations have been performed showing good qualitative agreement

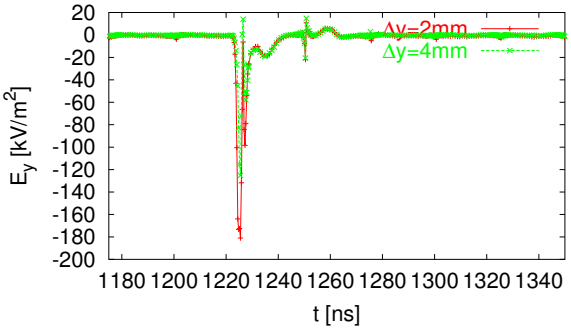

Figure 22: Simulated bunch-to-bunch wake field for the SPS. The bunch at time 1225 ns is displaced and the following bunch at about 1250 ns experiences a resulting force, which scales roughly linearly with the displacement, so that the wake field is uniquely defined.

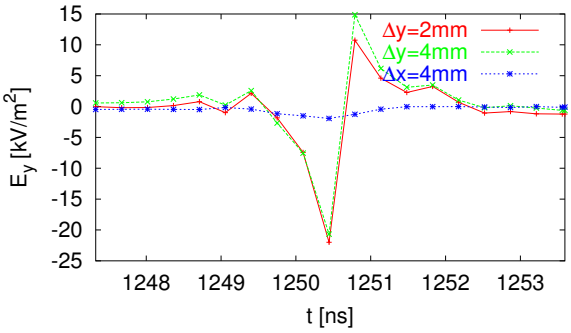

Figure 23: Simulated bunch-to-bunch wake field for the SPS. Zoomed view of the next-bunch wake of Fig. 22. The wake changes sign inside the bunch. The force scales linearly with the displacement, so that the wake field is uniquely defined, and there is little cross talk between the two planes.

in most cases. Quantitative results are not in perfect agreement. We demonstrated the importance to take the scrubbing history into account.

AKNOWELEDGMENTS

The authors would like to thank G. Arduini for providing them with the beam parameters for the different measurements, V. Baglin, B. Jenninger, J. M. Jiménez, J.-M. Laurent and A. Rossi for the data of the measurements and F. Ruggiero for his support and useful discussion.

REFERENCES

[1] Main contributors to the code were in chronological order): F. Zimmermann, O. Brüning, X.-L. Zhang, G. Rumolo, D. Schulte, and G. Bellodi.

[2] F. Zimmermann, "A Simulation Study of Electron-Cloud Instability and Beam-Induced Multipacting in the LHC," CERN LHC Project Report 95 (1997).

[3] O. Brüning, "Simulations for the Beam-Induced Electron Cloud in the LHC beam screen with Magnetic Field and Image Charges," CERN LHC Project Report 158 (1997).

[4] G. Rumolo, F. Ruggiero, F. Zimmermann, "Simulationm of the electron Cloud Build Up and its Consequences on Heat Load, Beam Stability and Diagnostics," PRST-AB 4, 012801 (2001).

[5] F. Zimmermann, "Electron Cloud Simulations: An Update," Proc. Chamonix 2001, CERN-SL-2001-003 DI (2001).

[6] See also World-wide web page on "Electron Cloud in the LHC" at the address `http://wwwslap.cern.ch/collective/electron-cloud/`.

[7] G. Arduini. Private communication.

[8] M. Furman and G. Lambertson, "The Electron-Cloud Instability in the Arcs of the PEP-II Positron Ring," Proc. Int. Workshop on Multibunch Instabilities in Future Electron and Positron Accelerators (MBI 97), Tsukuba, KEK, KEK Proceedings 97-17 (1997).

[9] R. Kirby and F. King, "Secondary Electron Emission from Accelerator Materials," 8th ICFA Beam Dynamics Mini-Workshop on 'Two-Stream Instabilities', SLAC-PUB-8380 (2000).

[10] N. Hilleret, private communication (2003) and "SEY and Pick-up Calorimeter Measurements," Mini-Workshop on 'SPS Scrubbing Run Results and Implications for the LHC', CERN, 28 June 2002, `http://sl.web.cern.ch/SL/sli/Scrubbing-2002/Workshop.htm`.

[11] N. Hilleret, "SEY measurements during the scrubbing run," minutes of the CERN Accelerator Performance Committe meeting of 01.08.2003, `http://ab-div.web.cern.ch/ab-div/Meetings/APC/`.

[12] V. Baglin, et al., "A Summary of the Main Experimental Results Concerning the Secondary Electron Emission of Copper," CERN LHC Project Report 472 (2002).

[13] H. Seiler, "Secondary Electron Emission in the Scanning Electron Microscope," J. Appl. Phys. **54**, 11 (1983).

[14] R. Cimino, I.R. Collins et al., "Can Low Energy Electrons Affect High Energy Physics Accelerators?," CERN-AB-2004-012 (ABP), submitted to Phys. Rev. Letters (2003).

[15] M. Blaskiewicz, private communication (2003).

[16] J.M. Jiménez et al., "Electron Cloud with LHC-Type Beams in the SPS: A Review of Three Years of Measurements," CERN LHC PRoject Report 632, and Proc. ECLOUD'02, CERN, Geneva, Switzerland, CERN-2002-001 (2002).

[17] J.M. Jiménez, "Electron Cloud and Vacuum Effects in the SPS," these proceedings.

[18] V. Baglin, B. Jenninger, "SPS Electron-Cloud Heat Load Measurements with WAMPAC and Simulations," Proc. ECLOUD'02, CERN, Geneva, Switzerland, CERN-2002-001 (2002).

[19] K. Ohmi, "Beam-Photoelectron Interactions in Positron Storage Rings," Phys. Rev. Letters 75, 8 (1995).